Lawrence Berkeley National Laboratory
LBL Publications

Title

Design Principles in Engineering of Multigrain Nanocatalysts via Multiscale Electronic Structure Characterization

Permalink

https://escholarship.org/uc/item/7z93w325

Journal

Chemistry of Materials, 37(19)

ISSN

0897-4756

Authors

Cho, Min Gee
Ophus, Colin
Lee, Jung-Hoon
et al.

Publication Date

2025-10-14

DOI

10.1021/acs.chemmater.5c01154

Peer reviewed

eScholarship.org Powered by the California Digital Library
University of California

Design principles in engineering of multigrain nanocatalysts via multiscale electronic structure characterization

Authors: Min Gee Cho[1,2,3,4,5], Colin Ophus[6], Jung-Hoon Lee[7], Inchul Park[1,8], Dong Young Chung[1,9], Jeong Hyun Kim[1,2], Dokyoon Kim[10], Yung-Eun Sung[1,2], Kisuk Kang[1,8], Mary Scott[4,5], A. Paul Alivisatos[3,11,12,13], Taeghwan Hyeon[1,2]*, and Myoung Hwan Oh[11,12,14]*

Affiliations:

[1]Center for Nanoparticle Research, Institute for Basic Science (IBS), Seoul 08826, Republic of Korea.

[2]School of Chemical and Biological Engineering, and Institute of Chemical Processes, Seoul National University, Seoul 08826, Republic of Korea.

[3]Kavli Energy NanoScience Institute, University of California, Berkeley, and Lawrence Berkeley National Laboratory, Berkeley, California 94720, United States.

[4]National Center for Electron Microscopy (NCEM), Molecular Foundry, Lawrence Berkeley National Laboratory, Berkeley, California 94720, United States.

[5]Department of Materials Science and Engineering, University of California Berkeley, Berkeley, California 94720, United States.

[6]Department of Materials Science and Engineering, Stanford University, Stanford, California 94305, United States.

[7]Computational Science Research Center, Korea Institute of Science and Technology (KIST), Seoul 02792, Republic of Korea.

[8]Department of Materials Science and Engineering, Research Institute of Advanced Materials (RIAM), Seoul National University, Seoul 08826, Republic of Korea.

[9]Department of Chemical and Biomolecular Engineering, Korea Advanced Institute of Science and Technology (KAIST), Daejeon 34141, Republic of Korea.

[10]Department of Bionano Engineering and Bionanotechnology, Hanyang University, Ansan 15588, Republic of Korea.

[11]Department of Chemistry and Department of Materials Science and Engineering, University of California, Berkeley, California 94720, United States.

[12]Materials Sciences Division, Lawrence Berkeley National Laboratory, Berkeley, California 94720, United States.

[13]Department of Chemistry, The University of Chicago, Chicago, Illinois 60637, United States.

[14]Department of Energy Engineering, KENTECH Institute for Environmental and Climate Technology, Korea Institute of Energy Technology, Naju 58330, Republic of Korea.

*Correspondence: thyeon@snu.ac.kr (T.H.); mhoh@kentech.ac.kr (M.O.)

ABSTRACT

Engineering grain boundary (GB) strain provides a promising pathway to tune the catalytic properties of nanocrystals. However, structural heterogeneity from random grain orientation and geometry has limited clear structure–property correlations. Here, we utilize a multigrain Co_3O_4/Mn_3O_4 core/shell nanocrystal platform as a model system to systematically investigate how geometric misfit strain at GBs serves as catalytically active sites for the oxygen reduction reaction. Through precise subnanometer-level control over grain morphology and by integrating multiscale electronic structure characterization, we identify the electronic structural signature of GB defects and establish a direct correlation between localized strain fields and modified electronic states. Strain modulation at GBs alters the e_g orbital energy levels, with elongation along the *z*-axis combined with shear strain stabilizing the e_g states, in contrast to the destabilization observed under pure shear strain. This stabilization mechanism enhances the electrocatalytic activity and selectivity of strained GBs compared to strain-relaxed grain surfaces. Furthermore, we reveal that GBs exhibit a radial strain gradient, producing a spatial energy shift that further modulates local electronic structures, as resolved through classification of electron energy loss spectroscopy data. Together, these findings demonstrate that geometric misfit strain enables precise tuning of grain geometry and resulting electronic structures, offering a robust strategy for engineering next-generation nanocatalysts.

INTRODUCTION

Grain boundaries (GBs)[1,2] in nanocrystalline materials are of great importance due to their potential to yield unique electrical, optical, mechanical, and chemical properties[3-6]. These interfaces typically contain structural defects, such as dislocations and disordered atomic

arrangements, which induce localized strains and modify electronic structures. Capturing these structural features is a key step for establishing structure–property relationships and achieving desired functionalities[7-9]. However, GB structures often exhibit random orientations and configurations, presenting significant challenges for characterization and limiting the ability to directly correlate local atomic-scale defects with macroscopic material behavior. To address this complexity, we employ a "geometric misfit strain" framework[10] that differs from conventional two-dimensional (2D) epitaxial mismatch by enabling the formation of tilt boundaries at well-defined locations around nanocube cores. This approach allows systematic control of grain boundary structures and strain fields at the nanoscale.

Lattice mismatch in heterostructured nanocrystals has been widely shown to induce strain and structural distortions that can be harnessed to enhance material properties[11-18]. We previously demonstrated that geometric misfit strain in heterostructured multigrain nanocrystals provides a robust and reproducible platform for studying GB defects with precise structural control[10]. Utilizing cubic Co_3O_4 nanocrystals with uniform size and shape as cores, we synthesized well-ordered polycrystalline Mn_3O_4 shells, forming controlled tilt boundaries with tunable strain fields. Unlike typical epitaxial strain dominated by in-plane mismatch, geometric misfit strain arises from enforced gap-closing between adjacent shell grains, introducing out-of-plane and shear strain components.

Mn-oxo complexes have been widely studied as active sites in oxygen photo- and electrochemical catalysis for energy conversion applications[19,20]. A key strategy for optimizing catalytic performance has involved the synthesis of composite manganese oxides with various coordination geometries and oxidation states[21,22]. Previous studies have shown that catalytically active materials often have Mn^{3+} ions in edge-sharing octahedra with Jahn–Teller (J–T)

distortions[23,24]. To further enhance electrocatalytic activity, lattice engineering strategies[25-31], such as the growth of epitaxial thin-film composite oxides, have been employed to modulate the electronic structure at Mn octahedral sites, showing promise as non-precious metal catalysts[32,33]. However, these approaches primarily rely on composition tuning or 2D planar stress, which imposes intrinsic limitations on the extent to which electronic states can be modulated. Overcoming these limitations requires new modes of strain control that move beyond conventional epitaxy.

Building on the concept of geometric misfit strain, we explore its potential as a versatile tool for strain and defect engineering, deliberately introducing controlled three-dimensional distortions at GBs. While the structural advantages of geometric misfit strain are clear, its influence on material properties has yet to be explored.

Here, we systematically engineer GB defect structures in multigrain Co_3O_4/Mn_3O_4 nanocrystals, including control over GB number, GB thickness, and strain-relaxed island thickness, to elucidate how geometric misfit strain modulates local electronic structure and catalytic performance. Electron energy loss spectroscopy (EELS) and X-ray absorption spectroscopy (XAS) measurements reveal defect signatures associated with strained GBs, with strain-induced electronic modifications localized within the shell. By precisely tuning the shell thickness within the 1.5–2.5 nm range and adjusting shell morphology to expose predominantly {001} and {101} facets, we further confirm that the new peaks in the O K-edge originate from strained rather than strain-relaxed regions. By integrating high-resolution electron microscopy with unsupervised machine learning[34,35], we map the geometric variation of local electronic structures at subnanometer resolution. Furthermore, density functional theory (DFT) calculations reveal that the combined shear strain and bond elongation at GBs—characteristic of geometric misfit strain—

stabilizes the e_g orbital states, in contrast to the destabilization observed under pure shear strain, highlighting the distinct advantages of this strain mode for catalytic engineering.

RESULTS AND DISCUSSION

Geometric misfit strain and grain boundary engineering.

The formation of tilt boundaries and associated defects in Co_3O_4/Mn_3O_4 multigrain nanocrystals is mainly attributed to the geometric misfit strain between the grains of the tetragonal Mn_3O_4 phase, as schematically illustrated in Figure 1a. These multigrain nanocrystals were produced by depositing a body-centered tetragonal (bct) Mn_3O_4 shell onto face-centered cubic (fcc) Co_3O_4 nanocube cores. The known crystal structures of Co_3O_4 and Mn_3O_4 phases are cubic spinel (Fd-3m; a=b=c=8.084 Å, JCPDS #42-1467) and distorted spinel (I41/amd; a=b=5.765 Å, c=9.442 Å, JCPDS #80-0382), respectively, with the latter elongated along the *c*-axis. Due to the asymmetric lattice mismatch between Co_3O_4 and Mn_3O_4, the Co_3O_4 {100}/Mn_3O_4 {001} interface is energetically favored to minimize elastic strain energy (Figure 1a). As the Mn_3O_4 shell preferentially grows along its *c*-axis parallel to the Co_3O_4 [100], [010], and [001] zone axes, consequently, the *c*-axes of adjacent Mn_3O_4 grains on a Co_3O_4 nanocube are orthogonal. This geometric constraint at the cube edges induces lattice misorientation, creating a gap between lattices from neighboring grains. Estimation using the lattice parameters of bulk phases indicates that the angle between Mn_3O_4 (112) and (004) planes is ~49.2°, leading to a misorientation gap of ~8.4° between the Mn_3O_4 (112) planes in adjacent grains. The GB forms by closing this gap, generating normal and shear strains.

In this study, we used 11 nm-sized Co_3O_4 nanocubes as substrates, which are small enough to accommodate the epitaxial strain energy at the Co_3O_4/Mn_3O_4 interface, thereby minimizing

dislocation formation due to their edge length being shorter than the dislocation period[10]. At this size regime, the charge reconstructed Co_3O_4/Mn_3O_4 interface exists within ¼ unit cell length along the *c*-axis. Since GBs are localized within specific regions of the shell, the density of GB defects at the surface can be controlled by tuning the shell morphology, including thickness, faceting, and coverage, that is, the number of grains. As an extension of the Stranski-Krastanov (SK) growth mode, the tunability of the Mn_3O_4 shell in a multigrain nanocrystal can be categorized into three distinct regions: a geometric coherent layer (CL), grain boundary, and island (Figure 1a). The CL consists of a periodic 3D strain field, with GBs forming near the edges of the Co_3O_4 core, and is therefore designated as the "3D geometric CL" (ref. 10). Atop this strained layer is the island, with significant lattice relaxation. The tunable parameters for each domain include CL thickness (which inherently controls GB thickness), island thickness, and the number of grains (Figure 1b and Figure S1).

To systematically isolate these effects, we devised three sets of Co_3O_4/Mn_3O_4 multigrain nanocrystals: (i) a "CL-thickness control" set to vary GB thickness, (ii) an "island-formation" set to modulate strain relaxation, and (iii) a "pH-based" set to adjust the number of GBs. This design ensures we can examine how differences in GB density, thickness, and strain relaxation influence electronic structures in a controlled manner. To realize these sets experimentally, we controlled the growth mode of the Mn_3O_4 shell by varying synthetic parameters such as surface ligands and the amine/acid ratio in the reaction solution[10,36-38]. Transmission electron microscopy (TEM) characterization revealed distinct growth modes depending on the type of ligand used (Figures 1c and 1D). With a fixed growth mode, we monitored the evolution of shell morphology by varying the Mn precursor concentration.

Specifically, layer-by-layer growth in the Mn_3O_4 [001] direction was observed when formate ions were used as surface ligands (Figure 1c; CL1-3). As supersaturation levels increased, the geometric CL gradually thickened from 1.6 nm to 2.5 nm. According to the design principle[10], as the geometric CL thickens, both the thickness and surface area of the GBs increase, leading to an increase in strain (Figures 1b and 1c). It appears that formate ligands tend to stabilize the strained Mn_3O_4 {101} surface at GBs more effectively than chloride ligands, as evidenced by the geometric trend in the {101}/{002} surface ratio, which generally increases as the CL thickens.

For samples with varying island thickness, chloride ligands were used. The thickness and number of Mn_3O_4 islands increased with higher Mn precursor concentrations (Figure 1d; Island1-3). Since the island regions are enclosed by strain-relaxed {101} facets, increasing the island proportion results in a greater fraction of strain-relaxed surfaces. Chloride adsorption is insufficient to stabilize the strain energy, leading to island nucleation and growth as a means of strain relaxation[39]. Interestingly, unlike conventional epitaxial systems, the strain in this multigrain system increases as the coherent layer thickens, due to the growing volume of the gap at the shell/shell interface as it extends farther from the core edge. At thinner shells (Island1), the strain at the GB is relatively small, allowing the shell to accommodate the strain energy without island formation. However, as the shell thickens beyond a point where chloride ligands can no longer compensate for the accumulating geometric misfit strain energy, strain-relaxed {101}-faceted islands begin to develop.

Other than changing the thickness of GB and island, the number of grain boundaries can be controlled with pH (Figure 1e). The green-colored truncated square pyramids represent grains containing both CL and islands, formed under reaction conditions regulated by the amine/acid ratio. At the acidic condition, condensation reaction required for the formation of metal–oxygen–metal

bridge is less favorable, inhibiting the growth of oxides. At pH 7, the number of nucleation sites on the cube is limited, resulting in the growth of one to two grains per nanocrystal being dominant. At the basic condition, nucleation and growth are promoted, resulting in multiple GBs. The number of GBs in set (iii) follows the order: Island3 > less GB > shallow shell, in accordance with the amine/acid ratio.

Given that the dominant exposed surfaces of multigrain nanocrystals are Mn_3O_4 {101} planes, it is essential to measure strains perpendicular to these planes to fully understand their impact on catalytic properties. Although we previously reported that Mn_3O_4 lattice strains near the core edges increase with distance from the core[10], those measurements were limited to the <100> axis of the core, where the {101} surface planes of the shell are not visible. To capture the strain tensor in the {101} planes, we acquired high-angle annular dark-field scanning TEM (HAADF-STEM) image along the Co_3O_4 <110> direction (Figure 2). In Figure 2a, the gray-square-marked region indicates the area where the Mn_3O_4 shell overlaps with the Co_3O_4 core. We then calculated nanocrystal strain fields by performing geometric phase analysis (GPA)[40] on the fast Fourier transform (FFT) image, using the white-circled Bragg peaks shown in Figure 2b and employing Co_3O_4 as the reference lattice. In the resulting strain map (Figure 2b), the *x*-axis corresponds to the Mn_3O_4 [101] crystallographic direction, while the *y*-axis is oriented perpendicular to [101], aligning with the left surface of the top grain and the right surface of the bottom grain (as illustrated in Figure 2a). The strain components e_{yy} and e_{xy} represent the normal and shear strains of the Mn_3O_4 (101) plane, respectively (Figure 2b). Grain boundaries exhibit pronounced compressive strain relative to the strain-relaxed island regions near the grain centers, as highlighted by the white-circles in Figure 2b; the same behavior is evident in another GB enclosed by Mn_3O_4 (-101) surface planes in Figure 2c. The lattice distortion at the GB, evidenced by the opposite sign of e_{xy} for strain fields based on

Mn_3O_4 [101] and [-101], is illustrated in Figure 2d. These localized strains at the GBs lead to modifications in the electronic structure of the Mn_3O_4 shell.

Analysis of electronic structure landscape within strained nanocrystal

It is known that strains accompanying the local tetragonal deformation of metal octahedral (MO_6) units in transition metal oxide crystals are interrelated with the Jahn–Teller distortions, which significantly modify the electronic structure of the metal ions[41,42]. The ensemble electronic structure of Mn in each sample was measured using Mn K-edge X-ray absorption near-edge structure (XANES) and Mn $L_{2,3}$-edge XAS (Figures S2 and S3). The Mn K-edge spectrum of the "shallow shell" sample exhibits a higher average Mn oxidation state (~3.7), indicating charge reconstruction at the Co_3O_4/Mn_3O_4 interface (Figure S2). In the island-thickness control samples, as the Mn_3O_4 shell grows, the average Mn oxidation state—estimated by linear combination fitting of Mn K-edge spectra using Mn-based oxide references—decreases, approaching that of unstrained bulk Mn_3O_4. This trend is further supported by the deconvolution of Mn $L_{2,3}$-edge spectra, which shows that, as the island grows, its electronic structure resembles that of unstrained Mn_3O_4. On the other hand, for the geometric CL-thickness control samples, oxidation states derived from linear combination fitting remain relatively consistent across different shell thicknesses.

Although GPA analysis revealed a distribution of strain fields within the nanocrystal, suggesting potential local modifications in electronic structure, X-ray based bulk measurements captured only overall trends, missing detailed regional variations. This discrepancy underscores the need for high spatial resolution STEM-EELS analysis to resolve subtle, local electronic differences[35,43]. To compare Mn $L_{2,3}$-edge EELS spectra associated with geometric misfit strain and strain relaxation

across different regions, we measured the nanocrystals along the Co_3O_4 <100> zone axis for both island-free and island-containing samples (Figure 3 and Figures S4-S7). Due to the orientational relationship of the shell grains, when viewed along the Co_3O_4 <100> zone axis, all side Mn_3O_4 grains are projected along the <110> directions so that the Mn_3O_4 {112} grain boundary planes are parallel to the electron beam, thereby providing clearer geometric-dependent information (Figure 3a). As shown by summed spectra of specific pixels (Figures S5 and S6), spectral shapes vary depending on their location within the nanocrystal. A *K*-means clustering algorithm was applied to investigate these regional electronic structural characteristics (Figure 3b and Figure S7). To reduce the dimensionality of the clustering input, we first introduced a descriptor that captures the local strain state of Mn^{3+} ions. The contribution of strained Mn^{3+} ions to the spectral shape was resolved using simulated reference spectra generated with CTM4XAS[44] (Figure 3c and Figure S4). With a fixed amount of Mn^{2+} and Mn^{4+} ions, an increased proportion of strained Mn^{3+} ions causes the Mn L_3-edge in the simulated spectra to narrow and the ratio of the maximum Mn L_3-edge intensity to the intensity at 642.8 eV (denoted $I_{max}/I_{642.8eV}$), where the simulated unstrained Mn^{3+} curve peaks, to increase.

To ensure consistent class definitions across samples, we applied *K*-means clustering to the EELS spectra from pixels in nanocrystal regions of both island-free and island-containing samples. In the island-containing sample, classified pixels from top and side grains were displayed in separate EELS maps to account for differences in electron beam projection arising from their distinct crystallographic orientations. The resulting cluster centers, representing the average spectra for each class, along with their fits using simulated reference Mn ion spectra are shown in Figure 3d. Each spectrum was deconvoluted using a linear regression method for quantitative comparison[45,46]. The statistical distribution of pixels among classes varied between samples (Figure

3e): in the island-free sample, class 4 dominated, whereas in the top grain of the island-containing sample, class 1 prevailed. Analysis of the fractional contributions of various Mn ions in each class (Figure 3f) reveals that the sample without island is characterized by a high fraction of strained Mn^{3+} ions (class 4), while the sample with islands exhibits a higher proportion of unstrained Mn^{3+} ions in the top grain (class 1). Conversely, the pixel distribution in the side grains of the island-containing sample showed similar proportions of classes 1 and 4, indicating that both strain-relaxed and strained regions are present in comparable amounts. Although the cluster center spectra of classes 4 and 5 from the island-free sample in Figure 3d appear similar at first glance, linear fitting with simulated reference curves reveals subtle differences in Mn ion contributions.

Notably, when comparing side grains from different samples, the cluster center spectra of the same class exhibit similar shapes, yet subtle differences in Mn^{2+} and Mn^{4+} content lead to slight variations in Mn ion compositions. Moreover, even within a single sample, spectra belonging to the same class differ markedly between the top and side grains of the island-containing nanocrystal (Figure 3d), underscoring how crystallographic orientation shapes the observed electronic structure. Due to the grain geometry, top grains are projected perpendicular to Mn_3O_4 {004} planes, providing information along the *c*-axis, while side grains capture data perpendicular to it. For example, classes 1 and 2 in the top grain contain the highest fraction of unstrained Mn_3O_4, whereas the corresponding classes in the side grains, where {101} planes dominate the projection, display a much smaller proportion of unstrained Mn^{3+} than those in the top grain.

These observations confirm that the unique spectral line shapes originate from GB strain. While GB strain is still present in the island region, it is more relaxed, giving the island-containing sample a smaller proportion of strained regions than the island-free sample.

Detection and calculation of distorted octahedral Mn^{3+} sites by micro- and macroscale analyzes

To clarify the development of the Mn_3O_4 phase on the shallow shell surface, as well as the GB defects in the island-formation and CL-thickness control samples, we obtained O K-edge spectra (Figures 4a and 4b and Figure S8). Excitation of electrons from O 1s to partially occupied or unoccupied metal 3d orbitals provides electronic structure information of the nanocrystals up to ~10 nm, mostly within ~1 nm depth from the surface[47]. Compared with the metal 4sp–O 2p hybridization observed in the 540–545 eV range, the metal 3d–O 2p hybridization at 530–535 eV shows a relatively large variation among the CL-thickness control samples (Figure 4a). This indicates that the surface components of each sample differ significantly, while the surface coverage of the Mn_3O_4 phase varies only slightly. On the other hand, the metal 4sp–O 2p hybridization shows greater variation among the island-formation samples than the CL-thickness control samples. This implies that as the Mn concentration increases in the island-formation samples, the surface coverage of the Mn_3O_4 phase also increases significantly. For the Island1 sample, the low surface coverage of the Mn_3O_4 phase is evident, as the shape of the metal 4sp–O 2p hybridization peak more closely resembles that of Co_3O_4, and the pre-edge peak is similar to that of Co_3O_4 rather than Mn_3O_4. Additionally, the e_g peak of Mn_3O_4 (~533.4 eV) becomes more pronounced with increasing Mn concentration in both sample sets, confirming the development of the Mn_3O_4 phase.

Interestingly, new peaks at ~532.8 and ~535.5 eV (indicated by vertical dashed lines) emerged in the multigrain nanocrystal samples (Figure 4a). These peaks originate from GB defects, as they are not present in single-phase Co_3O_4 or Mn_3O_4 nanocrystals. In Figure 4b, we examined how the Mn L-edge and O K-edge evolve with increasing distance from the Co–Mn interface and analyzed

their correlation. This correlative study revealed that the ~532.8 eV feature is observed only in the CL region in the O K-edge EELS spectra, reinforcing the conclusion that the modified electronic structure originates primarily from the strained lattice in this region, rather than from the unstrained island region (Figure 4b and Figure S9). The CL region contains a higher proportion of strained Mn^{3+}, as confirmed by deconvolution of the Mn L-edge spectra. The XAS spectrum of CL3 in Figure 4a resembles that of the CL region in Figure S9, indicating that the characteristics of the CL3 surface are mostly derived from the CL region. Furthermore, the peak energies are in good agreement with those reported for manganese oxides containing electronically modified Mn^{3+} ions[48], supporting our XAS and EELS results indicating that the CL regions are enriched in Mn ions whose Mn^{3+} electronic structure differs from that of bulk Mn_3O_4.

We built a crystalline model for the unstrained Mn_3O_4 phase and its 3D strained state, incorporating both normal and shear strain by applying the closing gap of 8.4° between the Mn_3O_4 {112} planes. Using these model structures, we performed first-principles calculations to obtain the electronic density of states (DOS) for Mn_3O_4 under different strain conditions (Figure 4c and Figures S10–S13). The hybridized Mn 3d–O 2p states of both tetrahedral and octahedral Mn sites in strained lattices appear more delocalized compared to those in the unstrained phase. Notably, we attribute the emerging feature near 532.8 eV to electronic states arising from stabilization of the e_g orbitals at octahedral Mn^{3+} sites. To understand the origin of this stabilization, we analyzed the local DOS in regions of the tilted lattices. These regions exhibit both compressive and elongated distortions. In the compressive regions, both tetrahedral Mn d-states and octahedral e_g-states become destabilized relative to the unstrained structure. In contrast, in the elongated regions, the e_g orbitals of octahedral Mn sites are stabilized, an effect attributable to elongation along the *z*-axis (Figure S12), while the t_{2g} orbitals become slightly destabilized. Tetrahedral Mn sites in the

elongated regions exhibit minimal change. To isolate the role of shear, we also calculated the DOS under pure shear strain alone (Figure S13). In this case, no orbital stabilization was observed; rather, the orbitals were destabilized. These results confirm that the stabilization of the e_g orbitals originates from the combination of elongation and shear strain present in the tilted lattice of the geometric misfit GBs.

This localized electronic structure variation correlates with structural heterogeneity within the coherent layer (CL) of the shell. As the GB length increases, the unit cell at the GB gets larger[10], indicating greater local strain variation in thicker CLs. Since strain directly influences the electronic states, thicker CLs are expected to exhibit greater electronic structural diversity. This is supported by the increased full-width at half-maximum (FWHM) of the Gaussian fit to the defect peak at 532.8 eV in the O K-edge spectrum (Figure S8). In the CL-thickness control samples, the broadening of this peak with increasing CL thickness reflects growing electronic heterogeneity. In contrast, in the island-formation samples, the GB structure becomes more uniform with increasing Mn concentration, which we attribute to the greater coverage of strain-relaxing islands. The findings from soft and hard XAS, as well as EELS, can be summarized as follows: (1) In the CL-thickness control set, thicker CL samples have a greater population of electronically modified Mn^{3+} near the Mn_3O_4 {101} surface due to GB strain; (2) In the island-formation set, samples with more islands have a higher proportion of unstrained surface planes.

Correlating geometrically strained lattices with electrocatalytic activity

We investigated the effect of microstructural features of GB strain in core/shell nanocrystal on ORR performance using the sets of Co_3O_4/Mn_3O_4 multigrain nanocrystals under basic reaction conditions[15,49]. Single-phase Mn_3O_4 and Co_3O_4 nanocrystals were also tested as controls (Figures

5a-5c). Comparison of the polarization curves of Mn_3O_4 nanocrystals (grey) and shallow shell samples (black) indicates that weak J–T distortions, caused by the presence of Mn^{n+} (n>3) ions at the core/shell interface, have little effect on electrocatalytic activity, as reflected in the half-wave potential (Figure 5b). However, activity is enhanced as the CL regions develop on the shallow shell, as seen in the less GB (navy) and Island3 (red) samples. The highest activity is observed when there is no island on the nanocrystal surface and the CL is at its thickest (CL3; green). The trend among the CL-thickness control samples can be explained by the increasing proportions of strained {101} surface facets and the lowering of the e_g level as the CL thickens (CL1 < CL2 < CL3), which in turn reduces the calculated overpotential (see calculation in the following paragraph). On the other hand, the lower activity in the island-formation samples can be attributed to the relatively high ratio of unstrained Mn_3O_4 on the surface. The selectivity toward the 4-electron pathway is not high for the less GB samples, which have mostly unstrained island surfaces and seem to prefer the 2-electron pathway for the ORR, similar to reference Mn_3O_4 (Figure 5c). This observation is further supported by the shallow shell sample, which has no islands on the surface and shows a higher electron transfer number (n). The Island3 sample, with enhanced selectivity toward the 4-electron pathway, provides additional evidence of the GB effects. The CL3 sample demonstrates even higher activity and selectivity than the Island3 sample, due to the smaller proportion of unstrained regions in the shell. The phase of the Mn_3O_4 grains and their GB structures during electrochemical measurements showed good consistency, as confirmed by ex-situ Raman, in-situ extended X-ray absorption fine structure (EXAFS), and HRSTEM (Figures S14 and S15).

The effect of the strained lattice on ORR activity was further studied through DFT calculations[50-56] of the energetics of reaction intermediates (OOH*, O*, and OH*) on the Mn_3O_4

{101} surface (Figures 5d-5f and Figure S16). The Mn_3O_4 {001} surface was not investigated, as its behavior would be very similar to that of Mn_3O_4 nanocrystals based on previous strain tensor measurements[10] and the EELS results in Figures 3 and 4. The Mn_3O_4 {101} planes are the most strained and exposed facets of the multigrain nanocrystals, being orthogonal to the junctions of three adjacent grain boundaries. We first calculated the most stable surface stacking motif of Mn_3O_4 {101} under ORR electrochemical conditions, resulting in a layer of octahedral Mn^{3+} motifs passivated by OH surface ligands (Supplementary Table 1). We anticipate that the last step of the reaction ($OH^* + H^+ + e^- \rightarrow H_2O$) is rate-determining, as the adsorption energy of OH*, ΔG_{OH^*}, is negative relative to that of H_2O. However, as the aspect ratio ($c/\sqrt{2}a$) of the unit cell decreases by systematically increasing and decreasing the lattice parameters a and c, respectively, in the strained lattice, ΔG_{OH^*} is significantly altered, rendering the desorption of OH* thermodynamically favorable and thereby increasing the operating potential (Figures 5e and 5f). These findings strongly support our experimental observation of enhanced ORR activity in the strained lattice at the CLs of Mn_3O_4 grains, which is comparable to or even surpasses that of previously reported strain-controlled Pt-based catalysts (Supplementary Table 2). By producing multigrain nanocrystals with more GBs (i.e., higher GB defect density) and fewer islands (i.e., lesser strain-relaxed surface), and by controlling GB thickness to achieve optimal strain, the surface proportion of strained lattice can be increased, offering further opportunities to maximize catalytic activity.

CONCLUSION

This work represents a breakthrough in elucidating structure–property relationship of well-defined and well-patterned GB defects in heterostructured nanocrystals through rigorous

microscopic and macroscopic characterizations. By correlating strained lattice structures with electronic states, we have revealed that GB strain significantly enhances ORR activity. In our previous work, we demonstrated that uniformly structured GB defects form at predetermined locations near the edges of nanocrystal cores, resulting from the highly constrained conditions imposed by the size and shape of the core and the symmetry and elasticity of the shell. These constraints induce a geometric misfit between adjacent shell lattices, distinct from traditional epitaxial strain at interfaces between different materials, offering a prior knowledge of the exact GB structure. In this study, we discovered that the grain structure is divided into several clearly differentiated regions, each with specific strain and electronic states determined by its interfaces, whether phase boundaries, grain boundaries, or surfaces. This knowledge, together with our ability to control grain growth modes, enables detailed nanoscale investigations of structure–property relationships and facilitates the rational design of nanocrystalline materials. Moreover, our approach is readily generalizable to other combinations of metals, metal oxides, and chalcogenides, opening avenues for exploring interfacial defect properties through geometrically regulated material deformations.

METHODS

Synthesis of the nanocrystals.

Monometallic Co_3O_4 and Mn_3O_4 nanocrystals as core materials.

The procedures are described in our previous paper[10].

CL-formation samples[10].

A mixture of oleylamine (5 mmol), oleic acid (0.5 mmol), and hydrochloric acid (3.15 mmol, Aldrich) to 15 mL of *o*-xylene (Aldrich) containing 0.080 g of Co_3O_4 nanocubes were prepared. As-prepared suspension was heated to 60 °C under air and aged for 1 h. After that, 4 mL of 0.125 (CL1), 0.25 (CL2), and 0.5 M (CL3) aqueous solution of Mn (II) formate was rapidly injected into the suspension at 90 °C and aged for 1.5 h. After the reaction, the nanocrystals were washed with hexane and ethanol and retrieved by centrifugation. And then the nanocrystals are well dispersed in non-polar solvents.

island-formation samples[10].

The synthetic procedure is the same as that for CL-formation samples except that Mn (II) chloride (Aldrich) (0.8 mL of 0.25 (Island1), 0.63 (Island2), and 2.5 M (Island3)) and xylenes (Aldrich) were used instead of Mn (II) formate and *o*-xylene. For the EELS measurement, this procedure was repeated for three times.

GB-formation samples[10].

For shallow shell sample, the procedure is the same as that for Island3 sample except that 4 mmol of oleylamine was used. The synthetic procedure is the same as that for Island3 except that 4.5 mmol of hydrochloric acid was used instead of 3.15 mmol of hydrochloric acid.

Electron Microscopy, Spectroscopy, and X-ray-based Experimental Methods.

The transmission electron microscopy (TEM) images were obtained using a JEOL JEM-2100F at 200 kV. The EFTEM images were recorded with a JEOL JEM-2100F. HAADF-STEM images and corresponding EELS data were obtained by using JEM-ARM200F operated at 200 kV (Cold Field Emission Type, JEOL) in National Center for Inter-university Research Facilities (NCIRF), Seoul National University. JEM-ARM200F microscope is equipped with 965 GIF Quantum ER (GATAN) EELS detector. Energy windows used for Mn L-edge map and Co L-edge map are 635.2–661.2 eV and 773–804 eV, respectively. Background is subtracted by the window of ~620 eV (width ~18 eV) for Mn and 750 eV (width ~25 eV) for Co. For HAADF-STEM imaging and EELS spectra, we adopted a convergence semi-angle and inner detect collection angle of 19 mrad and 40 mrad, respectively. Pixel time used to acquire HAADF-STEM image was 31.7 μs. Elemental analysis was performed via inductively coupled plasma- atomic emission spectroscopy (ICP-AES) (Shimadzu). HAADF-STEM image for strain mapping was acquired using TEAM0.5 at the NCEM facility at 200 kV, with a probe semi-angle of 30 mrad, a camara length of 0.105 m, and a C_2 aperture of 70 μm. X-ray diffraction patterns were obtained using a Rigaku D/max 2500 diffractometer equipped with a rotating anode and a Cu Kα radiation source (λ = 0.15418 nm). X-ray absorption near-edge structure (XANES) and soft X-ray absorption spectroscopy (XAS) experiments were carried out at 10C wide XAFS and 2A MS beamline,

respectively, in Pohang Light Source-II (PLS-II). Experiments at PLS-II were supported in part by MSIP and POSTECH.

GPA analysis.

Strain field maps were obtained using geometric phase analysis (GPA) implemented with a custom MATLAB script. Scan distortion, caused by sample motion relative to the STEM probe, leads to drift artifacts, most notably along the slow scan direction[57]. To quantify and correct this drift, we acquired scan pairs with the slow scan direction oriented at 0 and 90 degrees, enabling orthogonal comparison. Drift was measured and corrected using the method described in reference 57. GPA was then performed on the distortion-corrected image to extract strain information. The resulting strain maps follow standard infinitesimal strain definitions: normal strains in the x and y directions (e_{xx} and e_{yy}) and shear strain (e_{xy}). To visualize in-plane strain along the {101} planes, the x-axis was aligned with the {101} direction, and strain component along the y-axis was displayed. Finally, the strain maps were overlaid onto the original STEM images for visualization, with color representing the measured strain values.

***K*-means clustering of EELS data.**

For K-means clustering, we pre-excluded EELS spectra from background regions with the intensity threshold to investigate local variations of electronic structure within nanocrystal regions. For each pixel, we constructed a feature vector comprising two variables: (1) the maximum Mn L_3-edge intensity to the intensity at 642.8 eV ratio ($I_{max}/I_{642.8eV}$), and (2) the mean intensity scaled by a predefined constant to make the value comparable to intensity ratio values. For the $I_{max}/I_{642.8eV}$ ratio, I_{max} was defined as the maximum intensity observed within the L_3-edge window (638.7–646.7 eV). To mitigate noise-induced inconsistencies, the $I_{642.8eV}$ value was determined as the mean intensity within the 641.9–643.7 eV window, where the unstrained Mn^{3+} simulated spectrum exhibits its peak. Clustering was performed using scikit-learn's KMeans algorithm with a cluster number 6 ($K = 6$). The cluster labels were then separated into groups: the island-free sample and the top and side grains of island-containing sample.

Electrochemical measurements.

The ligand exchange procedure using nitrosonium tetrafluoroborate ($NOBF_4$) is as follows: 0.035 g of nitrosonium tetrafluoroborate was dissolved in 1.5 mL of dimethylformamide (DMF) in Ar atmosphere. This solution was added to the 10 mL of THF solution of as-prepared nanoparticles. Then the nanoparticles were precipitated by adding hexane, followed by centrifugation. After the ligand exchange, as-prepared nanoparticles were dispersed in ethanol and mixed with Vulcan XC-72 to load them onto a carbon support (nanocrystals/C). Nafion solution was mixed with nanocrystals/C dispersed in ethanol solution and loaded onto the rotating disk electrode (RDE, Autolab). Electrochemical experiments were conducted using a conventional three-compartment electrode system with a rotating ring-disk electrode (RRDE) (Pine, geometric area: 0.2475 cm^{-2}) and Autolab 302 potentiostat. Ag/AgCl and carbon rod were

used as a reference and counter electrode, respectively. All of the potentials are versus the reversible hydrogen electrode (RHE), and all of the electrochemical measurements were conducted in a 0.1 M KOH solution. The non-faradaic contribution during the oxygen reduction reaction (ORR) measurement was corrected by performing blank CV in Ar. The iR-correction was conducted based on the ohmic resistance measured by electrochemical impedance spectroscopy. The electron transfer number per oxygen molecule (n) was calculated from the RRDE method using the following equation (Ring disk potential was held at 1.4 V during the ORR measurement to oxidize hydrogen peroxide):

$$n = \frac{4\, I_d}{I_d + \frac{I_r}{N}}$$

where I_d is disk current, and I_r is ring current. N is the RRDE collection efficiency, which is 0.37 in our electrode.

DFT calculations

Computational Methods.

All calculations were performed within the generalized gradient approximation plus Hubbard U framework (GGA+U)[58]. The revised Perdew–Burke–Ernzerhof (RPBE) functional[59,60] for the exchange correlation to the density functional theory and projected augmented wave (PAW) method[61] was used as implemented in the Vienna *Ab initio* simulation package (VASP)[62]. The Hubbard U parameters (GGA+U) with U_{eff} =4.0 eV for Mn and U_{eff} =3.5 eV for Co were used to accurately calculate the electron correlation within the *d* states in the transition metal ions[63]. To avoid possible errors from different magnetic orderings, all the calculations employ ferromagnetic state model.

Adsorption energetics of ORR intermediates for Mn_3O_4 {011} surfaces were calculated with slab model with 3 metal sites per surface, 5 metal oxide thickness and more than 15 Å vacuum. The three topmost Mn_3O_4 layers were allowed to relax below the maximum force threshold of 0.05 eV/Å within an energy cutoff of 550 eV and a 3 × 3 × 1 gamma-point-centered *k*-point mesh. Solvation effects for ORR intermediates adsorbates were considered by exploiting the implicit solvation model[64].

Thermodynamics of Oxygen Reduction[65].

The individual steps in ORR mechanisms considered in this work are as follows: 4 electron reaction pathway with associative mechanism is

(1) $O_2 + H^+ + e^- \rightarrow OOH^*$

(2) $OOH^* + H^+ + e^- \rightarrow O^* + H_2O$

(3) $O^* + H^+ + e^- \rightarrow OH^*$

(4) $OH^* + H^+ + e^- \rightarrow {}^* + H_2O$

Gibbs free energy changes in oxygen reduction steps with associative mechanism are

$\Delta G_{a1} = \Delta G_{OOH^*} - 4.92\ [eV] + eU - \Delta G_{H^+}(pH)$

$\Delta G_{a2} = \Delta G_{O^*} - \Delta G_{OOH^*} + eU - \Delta G_{H^+}(pH)$

$\Delta G_{a3} = \Delta G_{OH^*} - \Delta G_{O^*} + eU - \Delta G_{H^+}(pH)$

$\Delta G_{a4} = - \Delta G_{OH*} + eU - \Delta G_{H^+}(pH)$

where U is the potential against Standard Hydrogen Electrode (SHE) at standard condition. The Gibbs free energy change of the proton relative to the pH is expressed by Nernst equation as $\Delta G_{H^+}(pH) = -k_B T \log(pH)$. Gibbs free energy change for individual step is represented by differences of DFT energy(E^{DFT}), zero-point energy(ZPE) and entropy between each step as $\Delta G_i = \Delta E_i + \Delta ZPE - T\Delta S$. To avoid calculation of O_2 energy, which is difficult to calculate accurately in GGA scheme, $\mathbf{\Sigma} G_{d1-3}$ and $\mathbf{\Sigma} G_{a1-4}$ are fixed to the experimental formation energy of H_2O, $2\Delta g^{exp}(2H_2 + O_2 \rightarrow 2H_2O) = - 4.92$ eV.

Adsorption energies of OH*, O*, and OOH* relative to H_2O and H_2 are calculated as

$\Delta E_{OH} = E(OH*) – E(*) – [E(H_2O) – 0.5\ E(H_2)]$

$\Delta E_{O} = E(O*) – E(*) – [E(H_2O) – E(H_2)]$

$\Delta E_{OOH} = E(OOH*) – E(*) – [2E(H_2O) – 1.5E(H_2)]$

ASSOCIATED CONTENT

Supporting Information.

The Supporting Information is available free of charge on the xxx website.

Comparative XRD, XANES, and soft-XAS analyses of geometry-controlled multigrain nanocrystals, STEM-EELS maps with and without island regions, Mn L-edge spectral deconvolutions, DFT calculation of strain effects on ORR, and Raman/EXAFS spectra collected before and after electrochemical testing (PDF)

AUTHOR INFORMATION

Corresponding Authors.

Taeghwan Hyeon – Center for Nanoparticle Research, Institute for Basic Science (IBS), Seoul 08826, Republic of Korea; School of Chemical and Biological Engineering, and Institute of Chemical Processes, Seoul National University, Seoul 08826, Republic of Korea; Email: thyeon@snu.ac.kr

Myoung Hwan Oh – Department of Chemistry and Department of Materials Science and Engineering, University of California, Berkeley, California 94720, United States; Materials Sciences Division, Lawrence Berkeley National Laboratory, Berkeley, California 94720, United States; Department of Energy Engineering, KENTECH Institute for Environmental and Climate Technology, Korea Institute of Energy Technology, Naju 58330, Republic of Korea; Email: mhoh@kentech.ac.kr

Authors.

Min Gee Cho – Center for Nanoparticle Research, Institute for Basic Science (IBS), Seoul 08826, Republic of Korea; School of Chemical and Biological Engineering, and Institute of Chemical Processes, Seoul National University, Seoul 08826, Republic of Korea; Kavli Energy NanoScience Institute, University of California, Berkeley, and Lawrence Berkeley National Laboratory, Berkeley, California 94720, United States; National Center for Electron Microscopy (NCEM), Molecular Foundry, Lawrence Berkeley National Laboratory, Berkeley, California 94720, United States; Department of Materials Science and Engineering, University of California Berkeley, Berkeley, California 94720, United States.

Colin Ophus – Department of Materials Science and Engineering, Stanford University, Stanford, California 94305, United States.

Jung-Hoon Lee – Computational Science Research Center, Korea Institute of Science and Technology (KIST), Seoul 02792, Republic of Korea.

Inchul Park – Center for Nanoparticle Research, Institute for Basic Science (IBS), Seoul 08826, Republic of Korea; Department of Materials Science and Engineering, Research Institute of Advanced Materials (RIAM), Seoul National University, Seoul 08826, Republic of Korea.

Dong Young Chung – Center for Nanoparticle Research, Institute for Basic Science (IBS), Seoul 08826, Republic of Korea; Department of Chemical and Biomolecular Engineering, Korea Advanced Institute of Science and Technology (KAIST), Daejeon 34141, Republic of Korea.

Jeong Hyun Kim – Center for Nanoparticle Research, Institute for Basic Science (IBS), Seoul 08826, Republic of Korea; School of Chemical and Biological Engineering, and Institute of Chemical Processes, Seoul National University, Seoul 08826, Republic of Korea.

Dokyoon Kim – Department of Bionano Engineering and Bionanotechnology, Hanyang University, Ansan 15588, Republic of Korea.

Yung-Eun Sung – Center for Nanoparticle Research, Institute for Basic Science (IBS), Seoul 08826, Republic of Korea; School of Chemical and Biological Engineering, and Institute of Chemical Processes, Seoul National University, Seoul 08826, Republic of Korea.

Kisuk Kang – Center for Nanoparticle Research, Institute for Basic Science (IBS), Seoul 08826, Republic of Korea; Department of Materials Science and Engineering, Research Institute of Advanced Materials (RIAM), Seoul National University, Seoul 08826, Republic of Korea.

Mary Scott – National Center for Electron Microscopy (NCEM), Molecular Foundry, Lawrence Berkeley National Laboratory, Berkeley, California 94720, United States; Department of Materials Science and Engineering, University of California Berkeley, Berkeley, California 94720, United States.

A. Paul Alivisatos – Kavli Energy NanoScience Institute, University of California, Berkeley, and Lawrence Berkeley National Laboratory, Berkeley, California 94720, United States; Department of Chemistry and Department of Materials Science and Engineering, University of California, Berkeley, California 94720, United States; Materials Sciences Division, Lawrence Berkeley National Laboratory, Berkeley, California 94720, United States; Department of Chemistry, The University of Chicago, Chicago, Illinois 60637, United States.

Author Contributions.

M.G.C., M.H.O., and T.H. conceived the research. M.G.C. and M.H.O. designed and performed the experiments and analyzed the results. C.O. provided the code for strain tensor measurements of the HAADF-STEM micrographs. J.-H.L. calculated density of states for strained oxide interfaces using DFT calculations. I.P. and K.K. performed DFT calculations for oxygen reduction reaction. D.Y.C. and Y.-E.S. carried out the electrochemical reactions. D.K. discussed and commented on the results. C.O. and M.C.S. advised the machine learning algorithm for analysis of EELS data. J.H.K. contributed in manuscript revision and provided critical advice that improved

the work. A.P.A. advised on the analysis of the experimental results. M.G.C. and M.H.O. wrote the manuscript. M.H.O. and T.H. supervised the project.

Notes.

The authors declare no competing financial interest.

Acknowledgments.

Synthesis and image analysis of the nanocrystal samples were supported by the Research Center Program of the IBS (IBS-R006-D1) (T.H.) and (IBS-R006-G1) (Y.–E.S. and K.K.) in Korea. Work at the Molecular Foundry was supported by the Office of Science, Office of Basic Energy Sciences, of the U.S. Department of Energy under Contract No. DE-AC02-05CH11231. M.C.S. and M.G.C. are funded by the U.S. Department of Energy through the program "4D Camera Distillery: From Massive Electron Microscopy Scattering Data to Useful Information with AI/ML. M.G.C. also acknowledges support from the Basic Science Research Program through the National Research Foundation of Korea (NRF) funded by the Ministry of Education (2021R1A6A3A14045275). Theoretical study at the Molecular Foundry was supported by the U.S. Department of Energy, Office of Science, Office of Basic Energy Sciences, Materials Sciences and Engineering Division, under Contract No. DE-AC02-05-CH11231 within the Physical Chemistry of Inorganic Nanostructures Program (KC3103) (A.P.A.). Computational resources were supported by the Supercomputing Center/Korea Institute of Science and Technology Information (KSC-2014-C3-037) (K.K.) and (KSC-2021-CRE-0430) (J.-H.L.). Work at KIST was supported by the KIST Institutional Program (2E31801) and the National Center for Materials Research Data (NCMRD) through the National Research Foundation of Korea funded by the Ministry of Science and ICT (2021M3A7C2089739). Basic Science Research Program through the NRF of Korea funded by the Ministry of Science, ICT & Future Planning (NRF-2019R1F1A1060107) (D.K.). Experiments at PLS-II were supported in part by MSIP and POSTECH.

References

1. Siegel, R. W.; Thomas, G. J. Grain Boundaries in Nanophase Materials. *Ultramicroscopy* **1992**, 40, 376–384.
2. Shen, J.; Aljarb, A.; Cai, Y.; Liu, X.; Min, J.; Wang, Y.; Wang, Q.; Zhang, C.; Chen, C.; Hakami, M.; **et al.** Engineering Grain Boundaries in Monolayer Molybdenum Disulfide for Efficient Water-Ion Separation. *Science* **2025**, *387*, 776–782.
3. Yazyev, O. V.; Louie, S. G. Electronic Transport in Polycrystalline Graphene. *Nat. Mater.* **2010**, *9*, 806–809.
4. Mariano, R. G.; McKelvey, K.; White, H. S.; Kanan, M. W. Selective Increase in CO_2 Electroreduction Activity at Grain-Boundary Surface Terminations. *Science* **2017**, *358*, 1187–1192.
5. Feng, X.; Jiang, K.; Fan, S.; Kanan, M. W. Grain-Boundary-Dependent CO_2 Electroreduction Activity. *J. Am. Chem. Soc.* **2015**, *137*, 4606–4609.
6. Talapin, D. V.; Lee, J.-S.; Kovalenko, M. V.; Shevchenko, E. V. Prospects of Colloidal Nanocrystals for Electronic and Optoelectronic Applications. *Chem. Rev.* **2010**, *110*, 389–458.
7. Wang, C.; Duan, H.; Chen, C.; Wu, P.; Qi, D.; Ye, H.; Jin, H. J.; Xin, H. L.; Du, K. Three-Dimensional Atomic Structure of Grain Boundaries Resolved by Atomic-Resolution Electron Tomography. *Matter* **2020**, *3*, 1999–2011.
8. Wang, Z.; Saito, M.; McKenna, K. P.; Gu, L.; Tsukimoto, S.; Shluger, A. L.; Ikuhara, Y. Atom-Resolved Imaging of Ordered Defect Superstructures at Individual Grain Boundaries. *Nature* **2011**, *479*, 380–383.
9. Mariano, R. G.; Kang, M.; Wahab, O. J.; McPherson, I. J.; Rabinowitz, J. A.; Unwin, P. R.; Kanan, M. W. Microstructural Origin of Locally Enhanced CO_2 Electroreduction Activity on Gold. *Nat. Mater.* **2021**, *20*, 1000–1006.
10. Oh, M. H.; Cho, M. G.; Chung, D. Y.; Park, I.; Kwon, Y. P.; Ophus, C.; Kim, D.; Kim, M. G.; Jeong, B.; Gu, X. W.; **et al.** Design and Synthesis of Multigrain Nanocrystals via Geometric Misfit Strain. *Nature* **2020**, *577*, 359–363.
11. Gamler, J. T. L.; Leonardi, A.; Sang, X.; Koczkur, K. M.; Unocic, R. R.; Engel, M.; Skrabalak, S. E. Effect of Lattice Mismatch and Shell Thickness on Strain in Core@Shell Nanocrystals. *Nanoscale Adv.* **2020**, *2*, 1105–1114.
12. Kwon, S. G.; Krylova, G.; Phillips, P. J.; Klie, R. F.; Chattopadhyay, S.; Shibata, T.; Bunel, E. E.; Liu, Y.; Prakapenka, V. B.; Lee, B.; **et al.** Heterogeneous Nucleation and Shape Transformation of Multicomponent Metallic Nanostructures. *Nat. Mater.* **2014**, *14*, 215–223.
13. Demortière, A.; Leonard, D. N.; Petkov, V.; Chapman, K.; Chattopadhyay, S.; She, C.; Cullen, D. A.; Shibata, T.; Pelton, M.; Shevchenko, E. V. Strain-Driven Stacking Faults in CdSe/CdS Core/Shell Nanorods. *J. Phys. Chem. Lett.* **2018**, *9*, 1900–1906.
14. Gu, F.; Wang, W.; Meng, H.; Liu, Y.; Zhuang, L.; Yu, H.; Chu, Y. Lattice Distortion Boosted Exceptional Electromagnetic Wave Absorption in High-Entropy Diborides. *Matter* **2025**, *8*, 102004.

15. Li, L.; Zhu, J.; Kong, F.; Wang, Y.; Kang, C.; Xu, M.; Du, C.; Yin, G. Tailoring Atomic Strain Environment for High-Performance Acidic Oxygen Reduction by Fe–Ru Dual Atoms Communicative Effect. *Matter* **2024**, *7*, 1517–1532.

16. Fairhurst, A. R.; Snyder, J.; Wang, C.; Strmcnik, D.; Stamenkovic, V. R. Electrocatalysis: From Planar Surfaces to Nanostructured Interfaces. *Chem. Rev.* **2025**, *125*, 1332–1419.

17. Bueno, S. L. A.; Leonardi, A.; Kar, N.; Chatterjee, K.; Zhan, X.; Chen, C.; Wang, Z.; Engel, M.; Fung, V.; Skrabalak, S. E. Quinary, Senary, and Septenary High-Entropy Alloy Nanoparticle Catalysts from Core@Shell Nanoparticles and the Significance of Intraparticle Heterogeneity. *ACS Nano* **2022**, *16*, 18873–18885.

18. Yao, Q.; Yu, Z.; Li, L.; Huang, X. Strain and Surface Engineering of Multicomponent Metallic Nanomaterials with Unconventional Phases. *Chem. Rev.* **2023**, *123*, 9676–9717.

19. Tsui, E. Y.; Tran, R.; Yano, J.; Agapie, T. Redox-Inactive Metals Modulate the Reduction Potential in Heterometallic Manganese-Oxido Clusters. *Nat. Chem.* **2013**, *5*, 293–299.

20. Hocking, R. K.; Brimblecombe, R.; Chang, L.-Y.; Singh, A.; Cheah, M. H.; Glover, C.; Casey, W. H.; Spiccia, L. Water-Oxidation Catalysis by Manganese in a Geochemical-Like Cycle. *Nat. Chem.* **2011**, *3*, 461–466.

21. Park, S.; Jin, K.; Lim, H. K.; Kim, J.; Cho, K. H.; Choi, S.; Seo, H.; Lee, M. Y.; Lee, Y. H.; Yoon, S.; **et al.** Spectroscopic Capture of a Low-Spin Mn(IV)-Oxo Species in Ni–Mn_3O_4 Nanoparticles during Water Oxidation Catalysis. *Nat. Commun.* **2020**, *11*, 1–10.

22. Yang, S.; Yue, K.; Liu, X.; Li, S.; Zheng, H.; Yan, Y.; Cao, R.; Zhang, W. Electrocatalytic Water Oxidation with Manganese Phosphates. *Nat. Commun.* **2024**, *15*, 1–13.

23. Du, J.; Zhang, T.; Cheng, F.; Chu, W.; Wu, Z.; Chen, J. Nonstoichiometric Perovskite $CaMnO_{3-\delta}$ for Oxygen Electrocatalysis with High Activity. *Inorg. Chem.* **2014**, *53*, 9106–9114.

24. Robinson, D. M.; Go, Y. B.; Mui, M.; Gardner, G.; Zhang, Z.; Mastrogiovanni, D.; Garfunkel, E.; Li, J.; Greenblatt, M.; Dismukes, G. C. Photochemical Water Oxidation by Crystalline Polymorphs of Manganese Oxides: Structural Requirements for Catalysis. *J. Am. Chem. Soc.* **2013**, *135*, 3494–3501.

25. Hou, Z.; Cui, C.; Li, Y.; Gao, Y.; Zhu, D.; Gu, Y.; Pan, G.; Zhu, Y.; Zhang, T. Lattice-Strain Engineering for Heterogenous Electrocatalytic Oxygen Evolution Reaction. *Adv. Mater.* **2023**, *35*, 1–48.

26. Wang, C.; Sang, X.; Gamler, J. T. L.; Chen, D. P.; Unocic, R. R.; Skrabalak, S. E. Facet-Dependent Deposition of Highly Strained Alloyed Shells on Intermetallic Nanoparticles for Enhanced Electrocatalysis. *Nano Lett.* **2017**, *17*, 5526–5532.

27. Wang, H.; Xu, S.; Tsai, C.; Li, Y.; Liu, C.; Zhao, J.; Liu, Y.; Yuan, H.; Abild-Pedersen, F.; Prinz, F. B.; **et al.** Direct and Continuous Strain Control of Catalysts with Tunable Battery Electrode Materials. *Science* **2016**, *354*, 1031–1036.

28. Bu, L.; Zhang, N.; Guo, S.; Zhang, X.; Li, J.; Yao, J.; Wu, T.; Lu, G.; Ma, J. Y.; Su, D.; **et al.** Biaxially Strained PtPb/Pt Core/Shell Nanoplate Boosts Oxygen Reduction Catalysis. *Science* **2016**, *354*, 1410–1414.

29. Strasser, P.; Koh, S.; Anniyev, T.; Greeley, J.; More, K.; Yu, C.; Liu, Z.; Kaya, S.; Nordlund, D.; Ogasawara, H.; **et al.** Lattice-Strain Control of the Activity in Dealloyed Core-Shell Fuel Cell Catalysts. *Nat. Chem.* **2010**, *2*, 454–460.

30. Liu, M.; Zhou, S.; Figueras-Valls, M.; Ding, Y.; Lyu, Z.; Mavrikakis, M.; Xia, Y. Compressively Strained and Interconnected Platinum Cones with Greatly Enhanced Activity and Durability toward Oxygen Reduction. *Adv. Funct. Mater.* **2024**, *34*, 1–8.

31. Liu, S.; Shi, C.; Xu, C.; Zhang, H.; Li, W.; Briega-Martos, V.; He, Q.; Han, Y.; Yang, Y. Epitaxial Growth of Atomic-Layer Cu on Pd Nanocatalysts for Electrochemical CO_2 Reduction. *Chem. Mater.* **2024**, *37*, 290–296.

32. Zeng, R.; Li, H.; Shi, Z.; Xu, L.; Meng, J.; Xu, W.; Wang, H.; Li, Q.; Pollock, C. J.; Lian, T.; **et al.** Origins of Enhanced Oxygen Reduction Activity of Transition Metal Nitrides. *Nat. Mater.* **2024**, *23*, 1695–1703.

33. Stoerzinger, K. A.; Risch, M.; Han, B.; Shao-Horn, Y. Recent Insights into Manganese Oxides in Catalyzing Oxygen Reduction Kinetics. *ACS Catal.* **2015**, *5*, 6021–6031.

34. Gleason, S. P.; Carbone, M. R.; Lu, D.; Ciston, J. Prediction of the Cu Oxidation State from EELS and XAS Spectra Using Supervised Machine Learning. *Microsc. Microanal.* **2024**, *30*, 1–10.

35. Blanco-Portals, J.; Peiró, F.; Estradé, S. Strategies for EELS Data Analysis: Introducing UMAP and HDBSCAN for Dimensionality Reduction and Clustering. *Microsc. Microanal.* **2022**, *28*, 109–122.

36. Skrabalak, S. E. Symmetry in Seeded Metal Nanocrystal Growth. *Accounts Mater. Res.* **2021**, *2*, 621–629.

37. Oh, M. H.; Yu, T.; Yu, S. H.; Lim, B.; Ko, K. T.; Willinger, M. G.; Seo, D. H.; Kim, B. H.; Cho, M. G.; Park, J. H.; **et al.** Galvanic Replacement Reactions in Metal Oxide Nanocrystals. *Science* **2013**, *340*, 964–968.

38. Choi, C. L.; Alivisatos, A. P. From Artificial Atoms to Nanocrystal Molecules: Preparation and Properties of More Complex Nanostructures. *Annu. Rev. Phys. Chem.* **2010**, *61*, 369–389.

39. Shklyaev, O. E.; Beck, M. J.; Asta, M.; Miksis, M. J.; Voorhees, P. W. Role of Strain-Dependent Surface Energies in Ge/Si(100) Island Formation. *Phys. Rev. Lett.* **2005**, *94*, 176102.

40. Hÿtch, M. J.; Snoeck, E.; Kilaas, R. Quantitative Measurement of Displacement and Strain Fields from HREM Micrographs. *Ultramicroscopy* **1998**, *74*, 131–146.

41. Gao, X.; Ikuhara, Y. H.; Fisher, C. A. J.; Moriwake, H.; Kuwabara, A.; Oki, H.; Kohama, K.; Yoshida, R.; Huang, R.; Ikuhara, Y. Structural Distortion and Compositional Gradients Adjacent to Epitaxial $LiMn_2O_4$ Thin Film Interfaces. *Adv. Mater. Interfaces* **2014**, *1*, 1400143.

42. Mori, S.; Chen, C. H.; Cheong, S.-W. Pairing of Charge-Ordered Stripes in $(La,Ca)MnO_3$. *Nature* **1998**, *392*, 473–476.

43. Chaupard, M.; Degrouard, J.; Li, X.; Stéphan, O.; Kociak, M.; Gref, R.; de Frutos, M. Nanoscale Multimodal Analysis of Sensitive Nanomaterials by Monochromated STEM-EELS in Low-Dose and Cryogenic Conditions. *ACS Nano* **2023**, *17*, 3452–3464.

44. Stavitski, E.; de Groot, F. M. F. The CTM4XAS Program for EELS and XAS Spectral Shape Analysis of Transition Metal L Edges. *Micron* **2010**, *41*, 687–694.

45. Friedman, J.; Hastie, T.; Tibshirani, R. Regularization Paths for Generalized Linear Models via Coordinate Descent. *J. Stat. Soft.* **2010**, *33*, 1–22.

46. Dahl, J. C.; Wang, X.; Huang, X.; Chan, E. M.; Alivisatos, A. P. Elucidating the Weakly Reversible Cs–Pb–Br Perovskite Nanocrystal Reaction Network with High-Throughput Maps and Transformations. *J. Am. Chem. Soc.* **2020**, *142*, 11915–11926.

47. Abbate, M.; Goedkoop, J. B.; de Groot, F. M. F.; Grioni, M.; Fuggle, J. C.; Hofmann, S.; Petersen, H.; Sacchi, M. Probing Depth of Soft X-Ray Absorption Spectroscopy Measured in Total-Electron-Yield Mode. *Surf. Interface Anal.* **1992**, *18*, 65–69.

48. Risch, M.; Stoerzinger, K. A.; Han, B.; Regier, T. Z.; Peak, D.; Sayed, S. Y.; Wei, C.; Xu, Z.; Shao-Horn, Y. Redox Processes of Manganese Oxide in Catalyzing Oxygen Evolution and Reduction: An *In Situ* Soft X-Ray Absorption Spectroscopy Study. *J. Phys. Chem. C* **2017**, *121*, 17682–17692.

49. Dubau, L.; Nelayah, J.; Moldovan, S.; Ersen, O.; Bordet, P.; Drnec, J.; Asset, T.; Chattot, R.; Maillard, F. Defects Do Catalysis: CO Monolayer Oxidation and Oxygen Reduction Reaction on Hollow PtNi/C Nanoparticles. *ACS Catal.* **2016**, *6*, 4673–4684.

50. Lin, L.; Ni, Y.; Shang, L.; Wang, L.; Yan, Z.; Zhao, Q.; Chen, J. Lattice-Strain-Induced Spin Regulation in Co–N/S Coordination-Framework Enhanced Oxygen Reduction Reaction. *Angew. Chem. Int. Ed.* **2024**, *63*, e202319518.

51. Lim, C.; Fairhurst, A. R.; Ransom, B. J.; Haering, D.; Stamenkovic, V. R. Role of Transition Metals in Pt Alloy Catalysts for the Oxygen Reduction Reaction. *ACS Catal.* **2023**, *13*, 14874–14893.

52. Jo, J.; Yoo, J. M.; Mok, D. H.; Jang, H. Y.; Kim, J.; Ko, W.; Yeom, K.; Bootharaju, M. S.; Back, S.; Sung, Y. E.; **et al.** Facet-Defined Strain-Free Spinel Oxide for Oxygen Reduction. *Nano Lett.* **2022**, *22*, 3636–3644.

53. Yang, X.; Wang, Y.; Tong, X.; Yang, N. Strain Engineering in Electrocatalysts: Fundamentals, Progress, and Perspectives. *Adv. Energy Mater.* **2022**, *12*, 2102261.

54. Seh, Z. W.; Kibsgaard, J.; Dickens, C. F.; Chorkendorff, I.; Nørskov, J. K.; Jaramillo, T. F. Combining Theory and Experiment in Electrocatalysis: Insights into Materials Design. *Science* **2017**, *355*, eaad4998.

55. Wang, L.; Zeng, Z; Gao, W.; Maxson, T.; Raciti, D.; Giroux, M.; Pan, X.; Wang, C.; Greeley, J. Tunable Intrinsic Strain in Two-Dimensional Transition Metal Electrocatalysts. *Science* **2019**, *363*, 870–874.

56. Luo, M.; Guo, S. Strain-Controlled Electrocatalysis on Multimetallic Nanomaterials. *Nat. Rev. Mater.* **2017**, *2*, 17059.

57. Ophus, C., Ciston, J., and Nelson, C.T. Correcting nonlinear drift distortion of scanning probe and scanning transmission electron microscopies from image pairs with orthogonal scan directions. *Ultramicroscopy* **162**, 1–9 (2016).

58. Mathew, K., Sundararaman, R., Letchworth-Weaver, K.., Arias, T. A. & Hennig, R. G. Implicit solvation model for density-functional study of nanocrystal surfaces and reaction pathways. *J. Chem. Phys.* **140**, 084106 (2014).

59. Nørskov, J. K. *et al*. Origin of the overpotential for oxygen reduction at a fuel-cell cathode. *J. Phys. Chem. B*. **108**, 17886–17892 (2004).

60. Anisimov, V. I., Aryasetiawan, F. & Lichtenstein, A. I. First-principles calculations of the electronic structure and spectra of strongly correlated systems: the LDA + U method. *J. Phys. Condens. Matter*. **9**, 767–808 (1997).

61. Perdew, J. P., Burke, K. & Ernzerhof, M. Generalized gradient approximation made simple. *Phys. Rev. Lett.* **77**, 3865–3868 (1996).

62. Hammer, B., Hansen, L. B. & Nørskov, J. K. Improved adsorption energetics within density-functional theory using revised Perdew-Burke-Ernzerhof functionals. *Phys. Rev. B*. **59**, 7413–7421 (1999).

63. Blöchl, P. E. Projector augmented-wave method. *Phys. Rev. B*. **50**, 17953–17979 (1994).

64. Kresse, G. & Hafner, J. *Ab initio* molecular dynamics for liquid metals. *Phys. Rev. B*. **47**, 558–561 (1993).

65. Wang, L., Maxisch, T. & Ceder, G. Oxidation energies of transition metal oxides within the GGA+U framework. *Phys. Rev. B*. **73**, 195107 (2006).

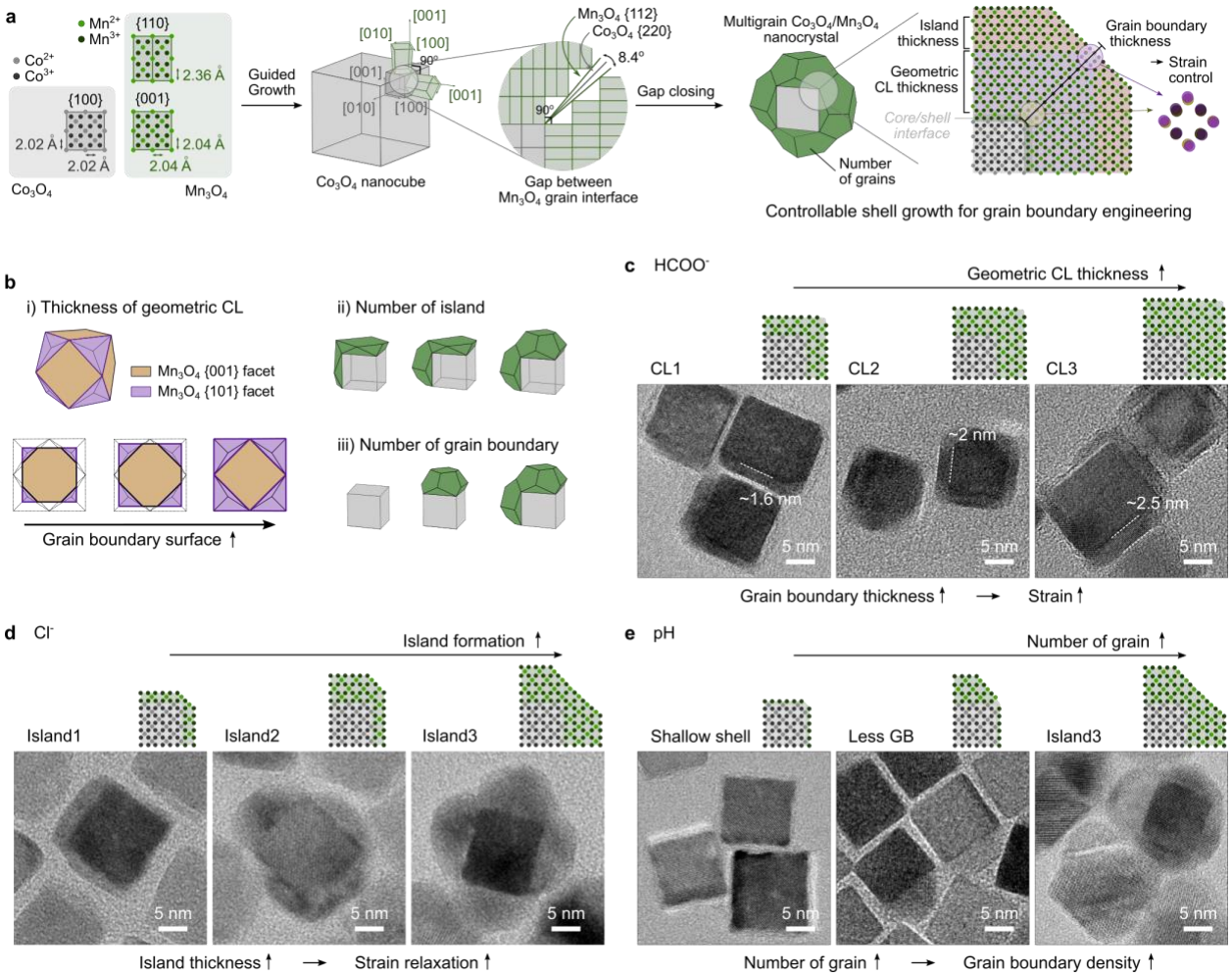

Figure 1. Engineering and controlling grain boundary defects in multigrain Co_3O_4/Mn_3O_4 core/shell nanocrystals. (a) Schematic illustration of the epitaxial and guided growth of Mn_3O_4 shell on a cubic Co_3O_4 core. Atomic arrangements in Co_3O_4 and Mn_3O_4 unit cells, viewed along the <100> direction for Co_3O_4 and along both the <110> and <001> directions for Mn_3O_4 (left). The orientational relationship between the Mn_3O_4 shell and Co_3O_4 core inducing a geometric misfit strain by gap closing, with an ~8.4° angle between two Mn_3O_4 {112} planes (middle). A 3D model and corresponding 2D illustration depict the controllable compartments in Mn_3O_4 grains, analogous to the SK growth mode (right). **(b)** Schematic illustration of grain geometry control. **(c-e)** TEM images of three distinct Mn_3O_4 grain morphologies obtained under different synthetic conditions. The CL thickness increases with higher manganese formate precursor concentration (**c**). The number of islands increases with higher manganese chloride precursor concentration (**d**). More GBs are formed with higher amine/acid ratios when using manganese chloride (**e**).

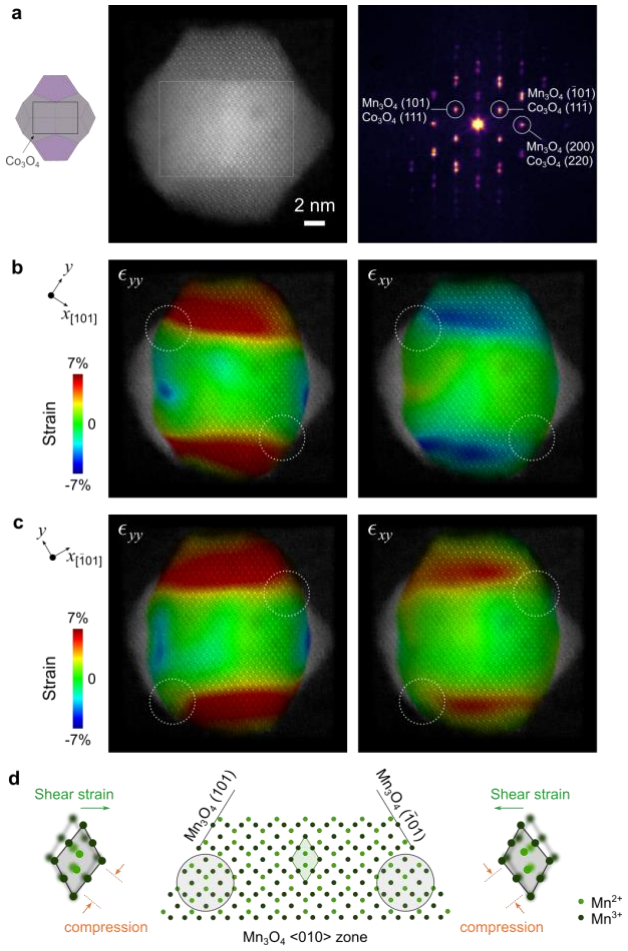

Figure 2. Strain measurement of multigrain nanocrystals. (a) Illustrative model, HAADF-STEM image, and corresponding FFT of a multigrain nanocrystal viewed along Co_3O_4 <110> zone axis. In the model, the top and bottom grains are shown in lavender, while the side grains are depicted in gray. The Co_3O_4 core region is marked with a gray square in HAADF-STEM image. **(b,c)** Strain tensor measurements taken in directions perpendicular to the Mn_3O_4 [101] (**b**) and [-101] (**c**) axes, visualizing compressive in-plane strains across the Mn_3O_4 {101} surface facets (white dotted circles). **(d)** Schematic illustration of the normal and shear strains induced within the framework of octahedral Mn^{3+} ions.

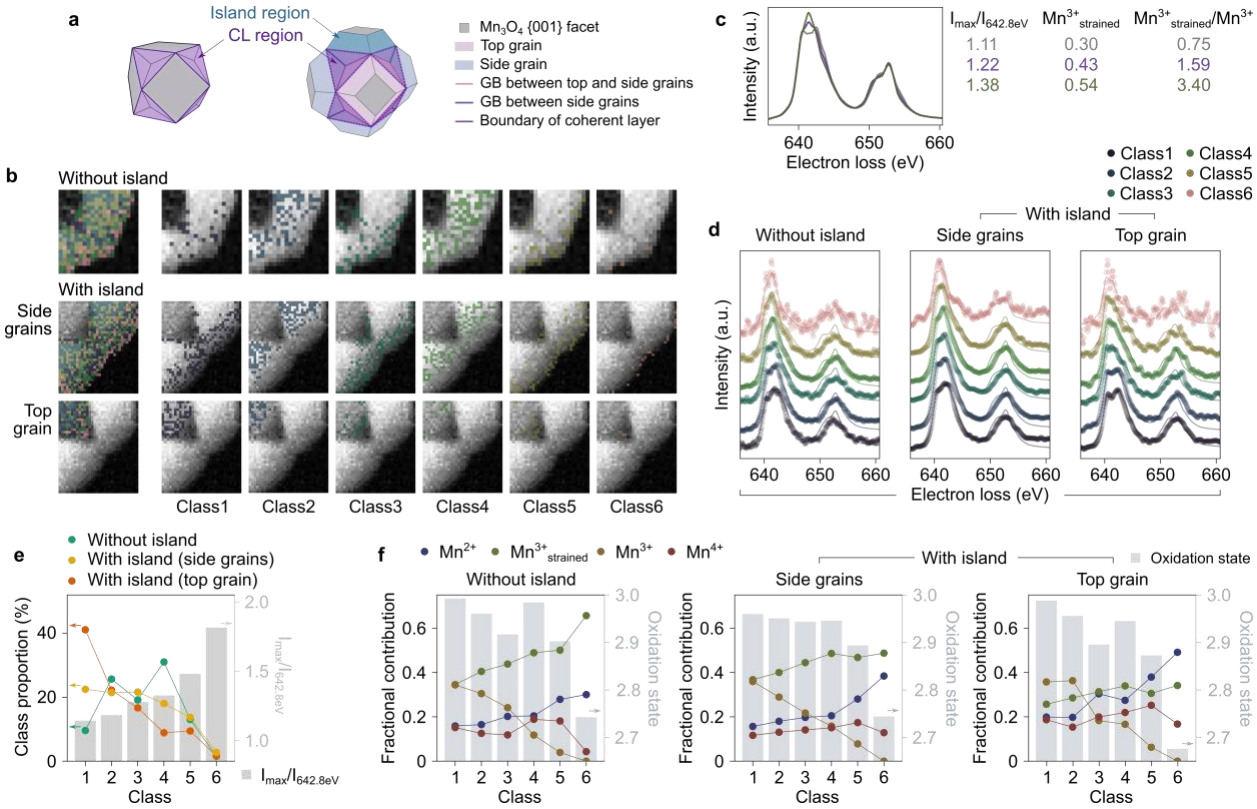

Figure 3. Local electronic structure characterization of Mn in different sub-grain regions. (a) Illustrations of the Co_3O_4/Mn_3O_4 nanocrystal morphology as viewed from the standard orientation of the Co_3O_4 core. All exposed facets are Mn_3O_4 {101} except for the grey-colored Mn_3O_4 {001} facets. **(b)** Mn $L_{2,3}$-edge EELS maps and *K*-means clustering results for samples without islands (first row) and with islands (second and third rows). Pixel sizes are 2.41 Å for the island-free sample and 3.65 Å for the island-containing sample. **(c)** Simulated spectra for strained Mn^{3+} ratios of 0.3, 0.43, and 0.54. **(d)** Experimental EELS spectra (dots) and their linear fits (lines) for the cluster centers of each class. The colors correspond to the clusters in *K*-means map. **(e)** Plot showing, for each sample, the proportion of pixels assigned to each class alongside the corresponding average $I_{max}/I_{642.8eV}$ ratio as a function of class number. **(f)** Fractional contributions (lines and circles) of reference spectra for Mn^{2+}, strained Mn^{3+}, unstrained Mn^{3+}, and Mn^{4+}, along with the oxidation state (light gray bars), plotted versus class number. These values were determined using Linear Regression coefficients from the fits in (**d**).

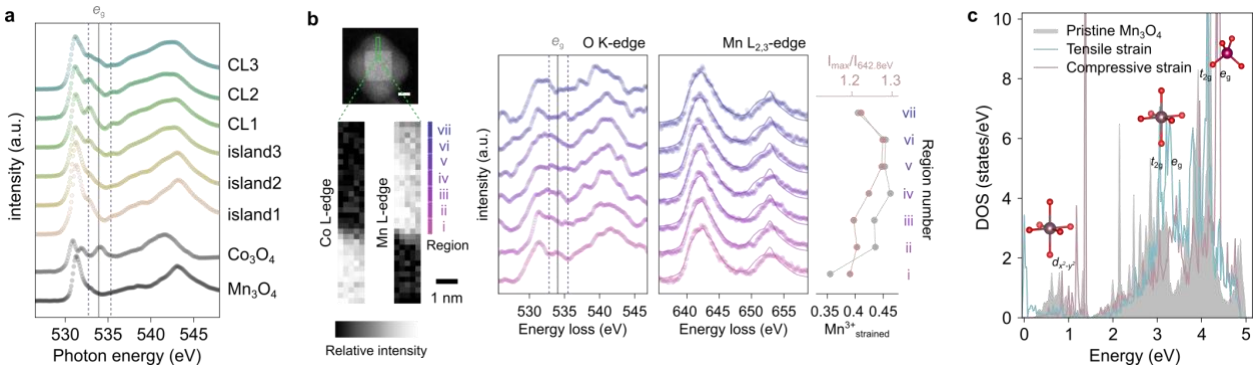

Figure 4. Capturing the surface electronic state of GB defects. (a) O K-edge spectra of monometallic Mn_3O_4 and Co_3O_4 nanocrystals and CL- and island-formation samples. **(b)** HAADF-STEM image, corresponding EELS elemental map, and EELS spectra of the sample with island. The pixel spacing for the EELS map is 2.5 Å. O K-edge EELS spectra from the regions of the near-interface between core and shell (i), the CL including the GB of the Mn_3O_4 shell (ii-vi), and the island of the Mn_3O_4 shell (vii). The dotted lines guiding the defect peaks at ~532.8 eV and ~535.5eV in (**a**) and (**b**). Experimental and simulation spectra are circles and line, respectively. The rightmost panel in (**b**) presents the relative fraction of strained Mn^{3+} ions and corresponding intensity ratios for each region. **(c)** DOS of pristine Mn_3O_4 and strained Mn_3O_4 after gap closing of {112} planes at the GB. The Fermi level is set to 0 eV.

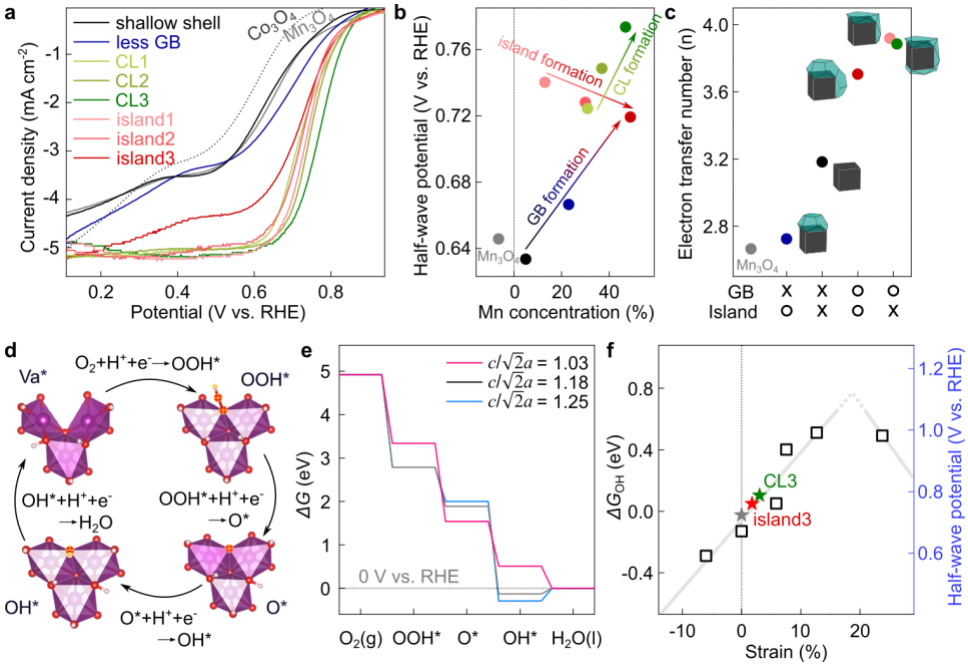

Figure 5. Revealing the effect of 3D strained lattice on electrocatalytic properties. (a-c) Electrocatalytic ORR activities of Co_3O_4, Mn_3O_4, and eight different types of Co_3O_4/Mn_3O_4 nanocrystals. Linear scan voltammogram was performed on a rotating disk electrode (1,600 rpm, 10 mV s^{-1} scan rate) in O_2-saturated 0.1M KOH solution (**a**). ORR activities presented in terms of half-wave potential (**b**) and electron transfer number (**c**). **(d-f)** DFT calculation results for the strain effect on the ORR activity of the Co_3O_4/Mn_3O_4 nanocrystals. Proposed ORR mechanism on Mn_3O_4 {101} plane (**d**). Free energy diagram (**e**) for ORR shows the changes in the binding energies of reaction intermediates when strain is imposed on the Mn_3O_4 {101} plane. For unstrained Mn_3O_4, the $c/\sqrt{2}a$ ratio is 1.18. Volcano plot of the ΔG_{OH} (eV) as a function of the calculated strain of Mn_3O_4 (**f**). Black open-squares and colored stars indicate the theoretical (black left *y*-axis) and experimental half-wave potentials (blue right *y*-axis), respectively.

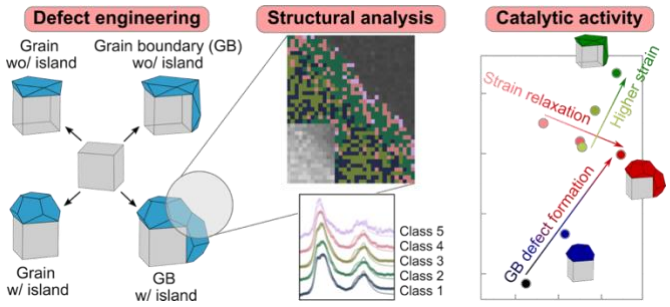
Defect engineering
Structural analysis
Catalytic activity
Grain
wo/ island
Grain boundary (GB)
wo/ island
Grain
w/ island
GB
w/ island
Class 5
Class 4
Class 3
Class 2
Class 1
Strain relaxation
Higher strain
GB defect formation